

Article

# Effect of Vacuum Annealing on the Nickel-Based Coatings Deposited on a CGI Cast Iron through Atmospheric Plasma Spraying

Peihu Gao <sup>1,2,\*</sup>, Baiyang Chen <sup>1,2</sup>, Shencong Zeng <sup>1,2</sup>, Zhong Yang <sup>1,2</sup>, Yongchun Guo <sup>1,2</sup>, Minxian Liang <sup>1,2</sup>, Tao Xu <sup>3</sup> and Jianping Li <sup>1,2,\*</sup>

<sup>1</sup> School of Materials and Chemical Engineering, Xi'an Technological University, Xi'an 710021, China; baiyang2578@163.com (B.C.); Z18889918364@163.com (S.Z.); yz750925@163.com (Z.Y.);

yc\_guo@163.com (Y.G.); gaoph@mail.xatu.edu.cn (M.L.)

<sup>2</sup> Shaanxi Province Engineering Research Centre of Aluminum/Magnesium Light Alloy and Composites, Xi'an 710021, China

<sup>3</sup> Technology Department, Xi'an Comboo New Materials Technology Co., Ltd., Xi'an 710032, China; xutao@163.com

\* Correspondence: tigersgaopei@163.com (P.G.); lijianping@mail.xatu.edu.cn (J.L.); Tel.: +86-29-8320-8080 (P.G.); +86-29-8617-3324 (J.L.)

Received: 28 June 2020; Accepted: 15 July 2020; Published: 16 July 2020



**Abstract:** Plasma-sprayed nickel-based self-fusion alloy coatings were annealed in a vacuum at 990, 1020 and 1050 °C for 20 min to increase the bonding between the compacted graphite cast iron substrate and coating, as well as the inner cohesion of the coatings. It was found that nickel and chromium diffused between nickel-based alloy coatings and compacted graphite cast iron substrate. A metallurgical transition zone with a thickness up to 1145 µm formed during the vacuum annealing, which resulted in an enhancement of the adhesion between the coating and substrate. The adhesion strength at room temperature was increased from the as-sprayed coating of 33.4 MPa to the annealed one of 163 MPa. Meanwhile, the adhesion strength at 500 °C reached 146 MPa. Conversely, the inner cohesion of the coating was improved with the particles' interfaces healed after vacuum annealing. The micro-hardness of the annealed coatings was increased to 902 HV from the as-sprayed one of 578 HV.

**Keywords:** vacuum annealing; nickel-based alloy coating; adhesion; cohesion; compacted graphite iron (CGI)

## 1. Introduction

Cast irons have been widely used as engineering parts [1–3]. Gray iron, compacted graphite iron and nodular iron are designed to serve in different circumstances. Compacted graphite iron has garnered more attention for its high strength, similar to nodular iron, and high thermal conductivity, comparable to the gray iron, while wear often takes place in compacted graphite iron engine parts, especially at high temperature [4–6]. Nickel-based alloys are widely used in anti-corrosion and wear-resistant applications for their excellent high-temperature properties [7–10]. Nickel and chromium are elements used at high temperature for their lower decrease of high temperature hardness than others. Boron and silicon are added into nickel and chromium alloy, not only to fabricate self-fluxing alloys, but also to form hard phases with nickel and chromium such as Ni<sub>3</sub>B and CrB. Nickel-based self-fusion alloy coatings offer both good anti-corrosion and good wear resistance [11–14].

Thermal spraying is often used to deposit nickel-based alloy coatings such as flame spray, atmospheric plasma spray (APS), high-velocity oxygen fuel (HVOF) spray, etc. [15–20]. Rapid melting

and solidification of the feedstock form splats and lamellar structures during thermal spraying. Moreover, pores, oxides and unmelted particles are usually brought into coatings which lead to a relatively low cohesion inside the coatings as well as adhesion between coating and substrate so as to lower the coating's mechanical performance [21–27].

Many works were carried out to re-melt the nickel-based alloy coatings. Li et al. [28] re-melted a plasma-sprayed NiCrBSi coating with a thickness of 800  $\mu\text{m}$  by TIG (T: tungsten; I: inert; G: gas). A bright area of transition zone formed between the coating and substrate with Fe, Ni and Cr diffusing near the interface as well as B and C diffusing inside the coating. Tian et al. [29] designed NiCr-Mo powders with a shell-core structure to enhance the adhesion strength of the Ni20Cr coating to 61.2 MPa. Bergant et al. [30,31] found that the adhesion between the coating and substrate was obviously enhanced after heat-treatment at 930  $^{\circ}\text{C}$ . Wen et al. [32] applied the vacuum re-melting on a supersonic atmospheric plasma-sprayed NiCrMoY coating to improve the wear resistance with much lower wear weight loss than the as-sprayed one. Meanwhile, the surface roughness was reduced by the low melting component liquid phase filling into the pores and cracks with improved coating density [33–36]. Moreover, annealing in a vacuum system could avoid the decarburization of the sensitive engine parts using, for example, vermicular cast iron and steel.

Flame, a common heat source, has been widely used to re-melt nickel self-fluxing alloy coatings to enhance adhesion between substrate and coating as well as cohesion inside coatings [35]. The flame torch has an uneven temperature distribution. During the re-melting process, all engine parts need to be heated to a certain temperature to trigger endothermic and exothermic processes. For example, if a valve seat coated with nickel self-fluxing alloy in a cylinder head is needed to trigger the self-fluxing process through oxygen-acetylene flame spray, the whole cylinder head needs to be heated up to a certain temperature. However, the temperature is distributed unevenly after flame heating, which would lead to some parts re-melting, especially at the corner of the parts with a complex shape. This would cause a flow curtain, which is formed when the coating is re-melted and parts of the re-melted coating flow over the substrate, especially at the corner or on an inclined plane. To avoid formation of a flow curtain and form the accurate re-melting, even heating is needed.

Therefore, vacuum annealing was adopted to re-melt the plasma-sprayed, nickel-based, self-fluxing alloys deposited on compacted graphite cast iron in this work. Effects of vacuum annealing on the coatings were investigated to enhance the coating's bonding.

## 2. Materials and Methods

### 2.1. Experimental Materials

Ni60 powders with a size ranging from 30 to 90  $\mu\text{m}$  were chosen as feedstock materials. The feedstock powders were prepared with atomized gas and had spherical morphologies, as shown in Figure 1, which were beneficial to the powder supply during plasma spraying.

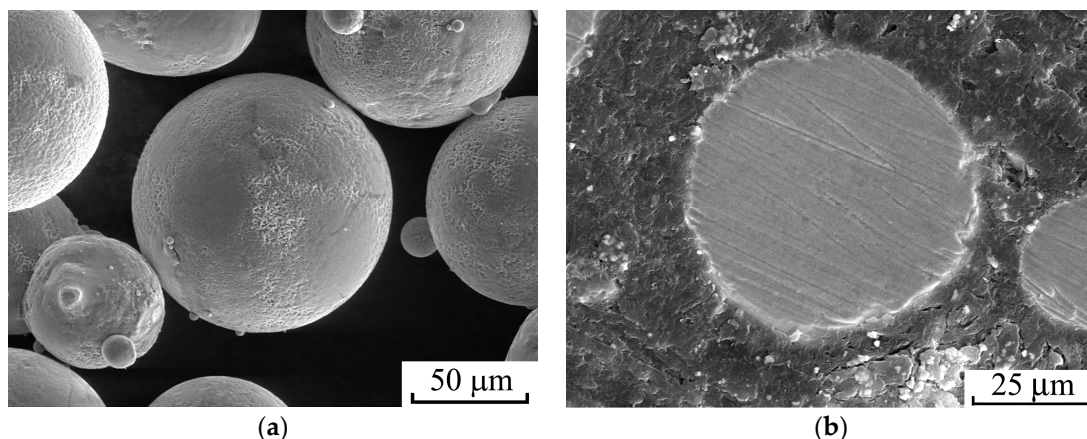


Figure 1. Morphology of Ni60 powders: (a) global; (b) cross-sectional.

The chemical composition of the Ni60 powder is listed in Table 1. In the powder, the weight contents of chromium, boron, silicon and iron were 17%, 4.2%, 4.8% and 12%, respectively. The balance was nickel. RuT300 compacted graphite cast iron (CGI) with the composition listed in Table 2 was selected as the substrate to investigate the adhesion between the CGI and nickel-based coating.

**Table 1.** Chemical composition of Ni60 powder.

Element	Cr	B	Si	Fe	Ni
wt.%	17	4.2	4.8	12	Bal.

**Table 2.** Chemical composition of RuT300.

Element	C	Si	Mn	P	S	Fe
wt.%	3.5	2.5	0.4	<0.07	<0.02	Bal.

## 2.2. Coating Deposition and Annealing

A plasma-spraying system of ZB-80 (Beijing Zhenbang Aerospace Co. Ltd., Beijing, China) was used with the plasma arc current and voltage of 550 A and 64 V. Argon was used as a primary plasma operating gas, and hydrogen was used as an auxiliary gas. During spraying, the pressures of both argon and hydrogen were fixed at 0.9 and 0.3 MPa, respectively. The spray distance was kept at 80 mm. Nitrogen was used as powder feed gas, and the powder feed rate was about 8 g/min. The coating deposition was operated with a 6-axis robot at a traversal speed of 300 mm/s. Before coating deposition, the vermicular cast iron substrate was sand-blasted with brown corundum.

The coatings were annealed at 990, 1020 and 1050 °C for 20 min with a stepped heating process when the temperature was higher than 850 °C within a vacuum environment, as shown in Figure 2. The pressure during the vacuum annealing was kept at  $10^{-1}$  Pa. The residual oxygen partial pressure was about  $2.1 \times 10^{-2}$  Pa. The main aim in adopting vacuum annealing was to avoid oxidation and decarburization of compacted graphite iron. The annealing temperature was chosen according to the nickel-based powder exothermal peak at about 1040 °C through differential scanning calorimetry (DSC) analysis provided by Chengdu Quanxin New Materials Co., Ltd. The accuracy of furnace temperature was calibrated to plus or minus three degrees, which would ensure the actual accuracy of vacuum annealing temperature.

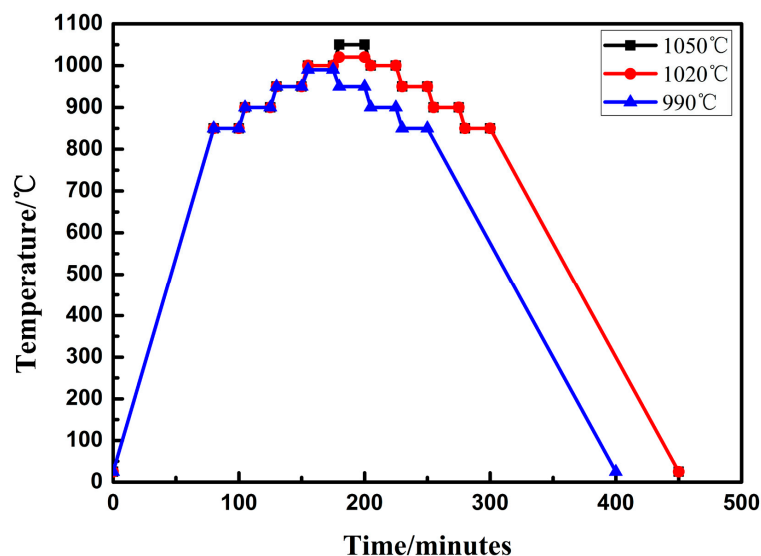


**Figure 2.** Vacuum annealing process of the coatings.

### 2.3. Characterization

The microstructures of the nickel-based powder and coating were characterized by scanning electron microscopy (SEM; VEGA II-XMU, TESCAN, Prague, Czech Republic). The phases were analyzed by X-ray diffraction (XRD-6000, Shimadzu, Kyoto, Japan) using Cu K $\alpha$  radiation. A surface roughness tester (C-KA9801KL, Tokyo Precision Instruments, Tokyo, Japan) was used to characterize the surface roughness of the coatings before and after vacuum annealing. The micro-hardness of the Ni60 coating was measured by a Vickers micro-hardness tester (HV-5, Taiming, Shanghai, China) under a load of 2 N for a loading duration of 30 s. Ten indentations were repeated. The mean micro-hardness and the standard deviation were calculated statistically.

Figure 3 shows the schematic of the adhesion strength testing. The adhesion strength of the coating was evaluated according to the ASTM C633-2013(2017) test standard. One of the two cylinder specimens was coated with nickel-based alloy; the other one was sand blasted. The two specimens were bonded with high-strength resin (E-7, Huayi Resins Co, Shanghai, China) for adhesion strength testing at room temperature as seen in Figure 3a. The strength of the E7 resin was about 70 MPa at room temperature. For the annealed coatings, the adhesion strength was higher than the strength of resin. Instead of high-strength resin, two cylinder specimens coated with Ni60 were placed together, with top coating face to face, and annealed at 990, 1020 and 1050 °C for 20 min in a vacuum with a stepped heating processing when the temperature was higher than 850 °C, as shown in Figure 2. After annealing, the two cylinder specimens with Ni60 coating were dissolved together to form a whole part which corresponded to the ASTM C633-2013(2017) test standard, as seen in Figure 3b. Both of the adhesion strengths at room temperature and 500 °C of annealed Ni60 coatings could be tested. The adhesion strength was tested through a universal strength testing machine (DDL300, Sinotest Equipment Co., Ltd., Changchun, China).

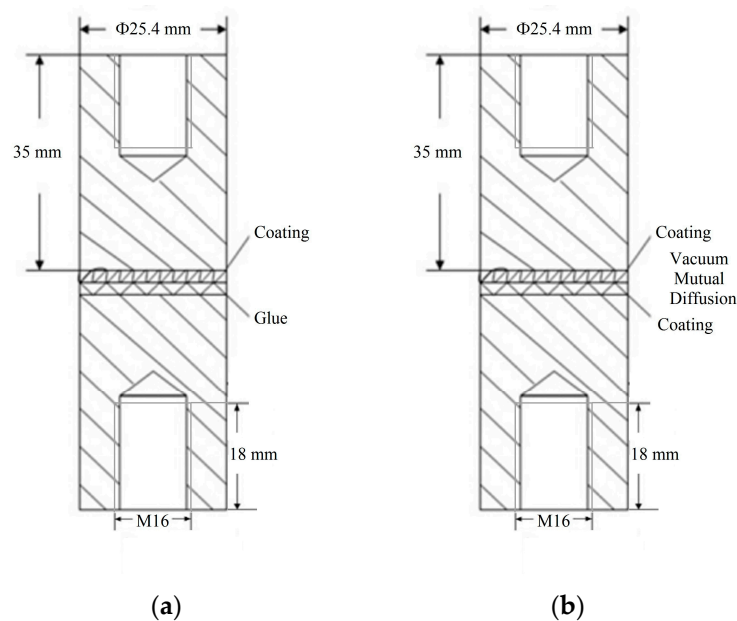


**Figure 3.** Schematic of adhesion strength testing: (a) room temperature; (b) high temperature.

## 3. Results and Discussion

### 3.1. Coating Microstructure and Interface Evolution

The cross-sectional microstructures of the as-sprayed and annealed coatings are shown in Figure 4. After annealing, the interlayer discontinuity between coatings and compacted graphite iron substrate disappeared. Meanwhile, a translation zone formed. Furthermore, the translation zone grew mainly towards the compacted graphite iron. In contrast, the translation zone was brighter than the nickel-based

coating, which is commonly known as diffusion transfer bright (DTB) [34,36]. The translation zone is often considered as a feature of metallurgical bonding [34,36]. The top surface of the nickel-based coating became smooth, which seemed like the coatings' surfaces re-melted through oxyacetylene flame, as compared to the as-sprayed one. After surface roughness testing, the Ra of the coatings before and after annealing were 22.6, 5.6, 4.5 and 4.3  $\mu\text{m}$ , respectively.

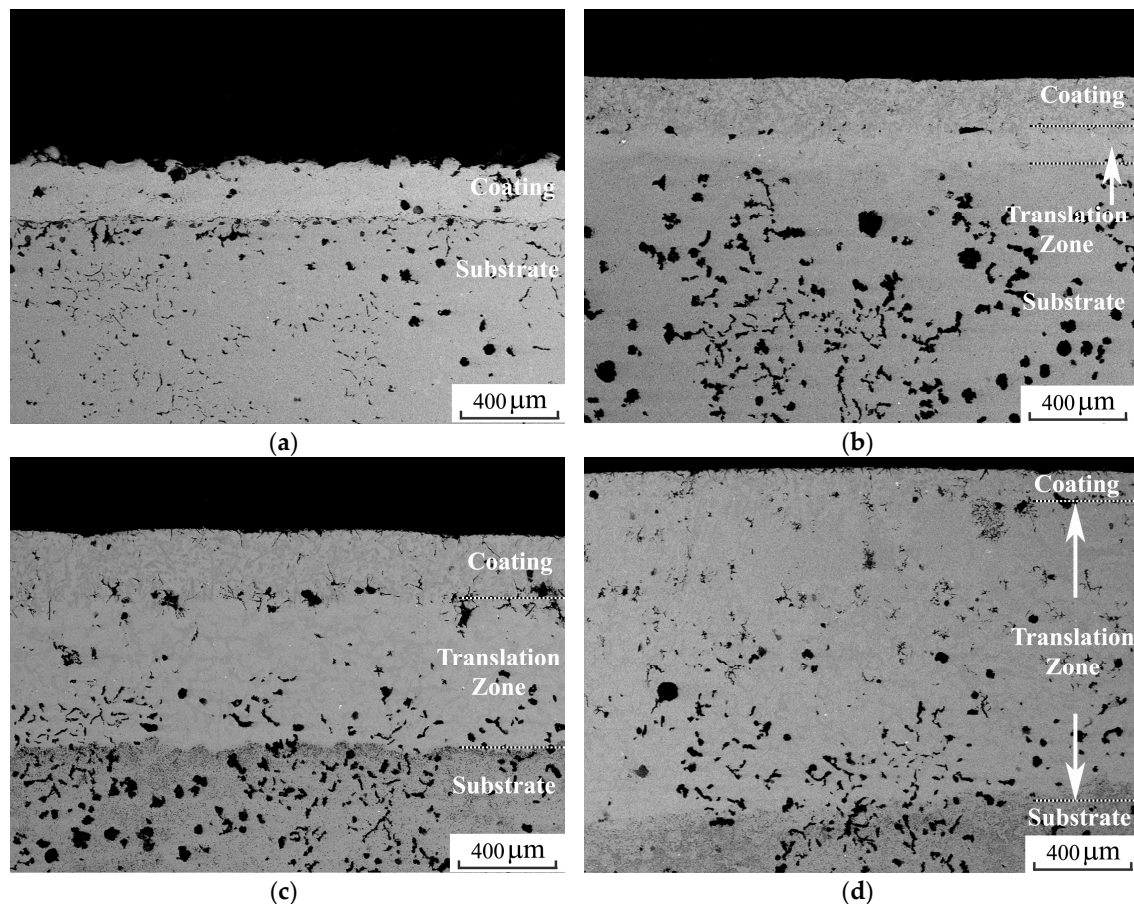


**Figure 4.** Cross-sectional microstructures of the coatings: (a) as-sprayed; vacuum annealed at (b) 990 °C; (c) 1020 °C; (d) 1050 °C.

It was found that there were evolutions of bonding between the compacted graphite iron substrate and the nickel-based coating from the as-sprayed one to the annealed. The thickness of the as-sprayed nickel-based coating was about 210  $\mu\text{m}$ . After annealing, the thickness of the translation zone increased from 134 to 672 to 1145  $\mu\text{m}$  as the annealing temperature increased from 990 to 1020 to 1050 °C. The translation zone thickness increased mainly towards the substrate direction at 990 and 1020 °C. When the temperature was increased to 1050 °C, the total thickness of the nickel-based coating and the translation zone was 1306  $\mu\text{m}$ ; the translation zone thickness was about 1145  $\mu\text{m}$ . The total thickness minus the translation zone thickness was about 161  $\mu\text{m}$ , which was lower than the as-sprayed thickness of 210  $\mu\text{m}$ . The coating elements diffused to the compacted graphite iron substrate and formed the translation zone, which finally led to the growth of the translation zone towards both the compacted graphite iron substrate and coating. The translation zone thicknesses of three annealed coatings are compared in Figure 5. The thicknesses of the coatings and translation zone are tallied in Table 3. The translation zone thickness increased linearly with the increase of annealing temperature. Furthermore, the formed diffusion transfer zone mainly diffused from the nickel-based alloy coating to the compacted graphite iron.

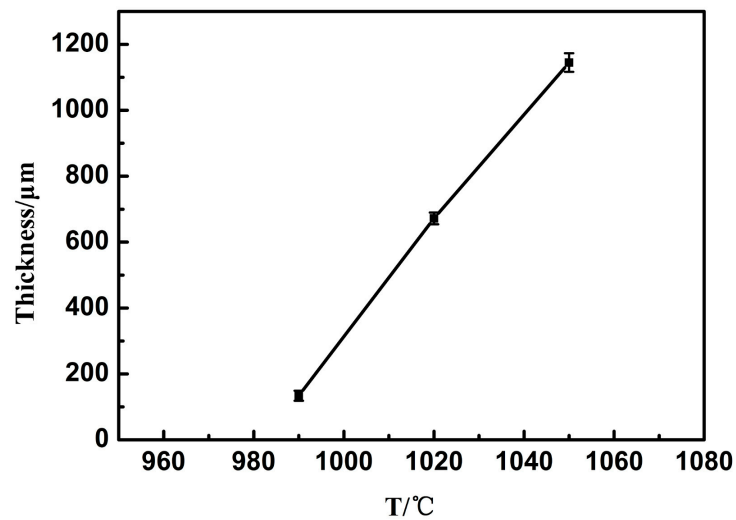


Figure 5. Relation of the transitional zone thickness to annealing temperature.

Table 3. Thickness of the coatings and translation zone.

Thickness/ $\mu\text{m}$ Deposit	As-Sprayed	990 °C	Annealed 1020 °C	1050 °C
Coating	210 $\pm$ 35	210 $\pm$ 15	210 $\pm$ 15	163 $\pm$ 28
Translation Zone	-	134 $\pm$ 15	672 $\pm$ 18	1145 $\pm$ 28
Total	210 $\pm$ 35	345 $\pm$ 15	883 $\pm$ 18	1306 $\pm$ 18

### 3.2. Element Analysis of Nearby Coating Interfaces

Figures 6 and 7 show the line analysis of elements in the as-sprayed and annealed coating at 990 °C for 20 min from the top of nickel-based coating to the CGI substrate across the interface. There were notable element contents of nickel, chromium and iron in the as-sprayed coating, which reflected the differences between the substrate and the coating. After annealing, the notable interlayer abruptly disappeared. Nickel and chromium contents increased in the CGI substrate. It was clear that nickel and chromium diffused into the substrate. Meanwhile, iron contents in the coating increased greatly, which reflected the iron diffused from substrate into nickel coating; thus, it was easier for Fe than other elements from the substrate to diffuse into the coating, and it was easier for nickel and chromium elements than other elements in the coating to diffuse into the compacted graphite iron substrate [37].

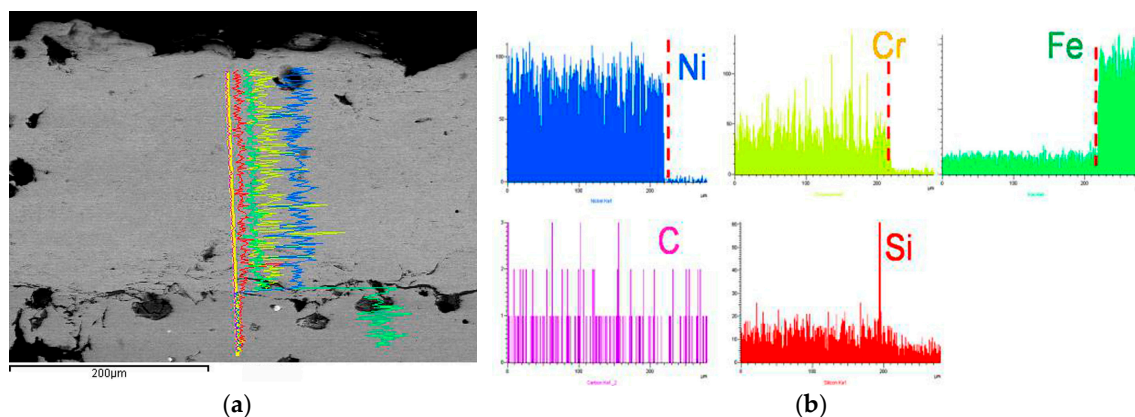
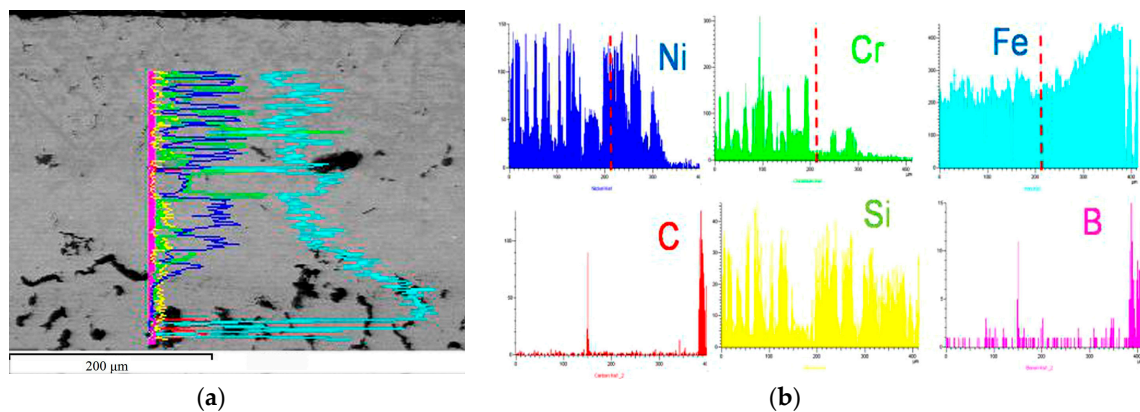
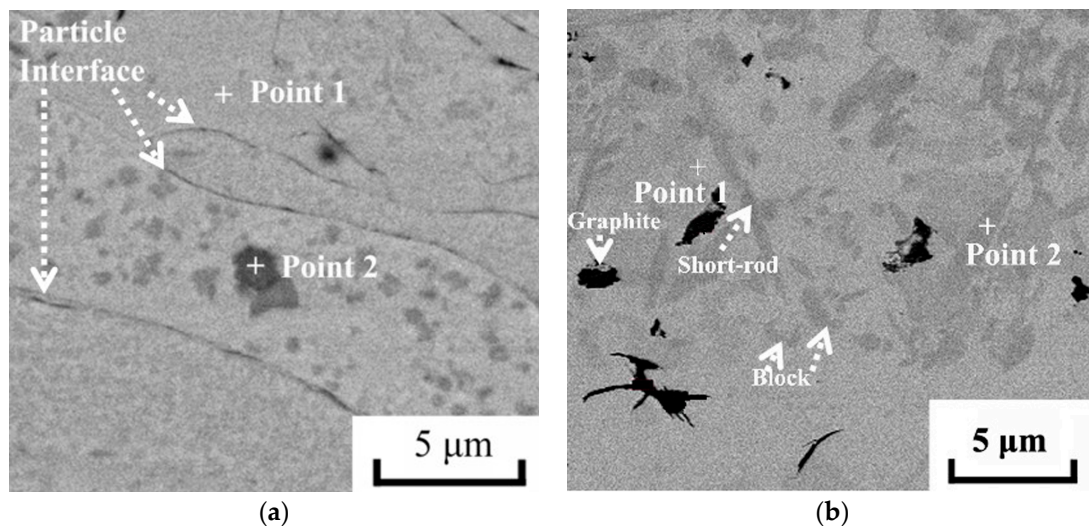


Figure 6. EDS element analysis of the as-sprayed Ni60 coating: (a) line analysis of elements; (b) element distribution along the line.



**Figure 7.** EDS element analysis of the Ni60 coating annealed at 990 °C for twenty minutes: (a) line analysis of elements; (b) element distribution along the line.

Figure 8 shows the cross-sectional microstructure of the as-sprayed coating and the annealed one at 990 °C for 20 min. There were lamellar structures and many particle interfaces in the as-sprayed coatings as shown in Figure 8a, which reflected the relatively poor cohesion among the as-sprayed coatings. Table 4 shows the element point analysis. The brighter field had higher nickel element contents, as shown at point 1 in Figure 8a. The darker precipitants had higher chromium and iron contents, as shown at point 2 in Figure 8a. After annealing, the particle interfaces disappeared, which improved the inner cohesions of the nickel coatings, as shown in Figure 8b. Short rod, block precipitants appeared. Table 5 shows the element point analysis of the annealed coating at 990 °C for 20 min. As compared to the as-sprayed one, in the brighter phases, nickel and chromium element contents decreased, and the iron element contents increased, which were consistent with the element line analysis results. Meanwhile, in the darker phases, the chromium precipitant content decreased, while the iron element content increased greatly, and some graphite precipitated as free carbon.



**Figure 8.** EDS point analysis of the as-sprayed coating (a) and the annealed one (b) at 990 °C for 20 min.

**Table 4.** EDS point analysis of the as-sprayed coating.

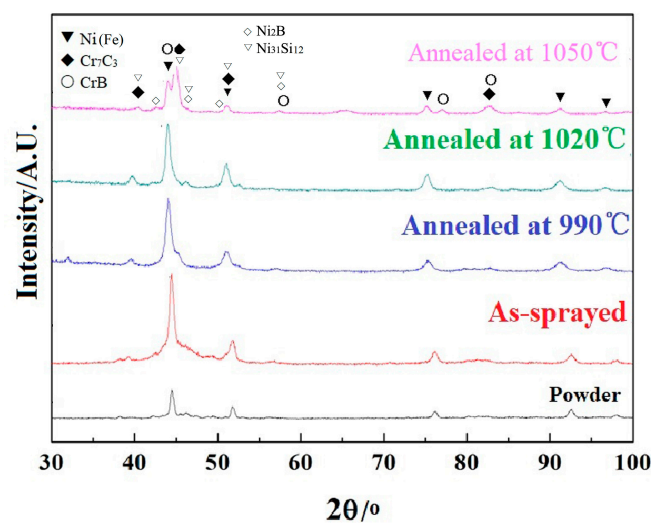
Element/wt.%	Ni	Fe	Cr	Si
Point 1	61.8	12.71	18.5	7.61
Point 2	31.2	14.43	46.96	2.72

**Table 5.** EDS point analysis of the annealed coating at 990 °C coating.

Element/wt. %	Ni	Fe	Cr	Si
Point 1	41.93	46.83	2.25	7.75
Point 2	7.73	60.92	30.23	-

### 3.3. Phase Composition

The phase compositions of the as-sprayed coating and re-melted coatings were characterized by XRD, as shown in Figure 9. In the feedstock, there was only a nickel peak, which was very obvious, and the other element peaks were not obvious. In the as-sprayed coating, iron dissolved into nickel, and  $\text{Ni}_{31}\text{Si}_{12}$  and  $\text{Ni}_2\text{B}$  phases precipitated. The results were similar to Wojciech Żórawski's work [38]. After annealing,  $\text{Cr}_7\text{C}_3$  and  $\text{CrB}$  phase peaks were obvious, which were helpful to strengthen the nickel alloy coating.

**Figure 9.** XRD analysis of the powder and coatings.

During the deposit of the as-sprayed coating, a large number of self-diffusion alloy coating elements, such as Cr, Si, B, Fe, etc., were dissolved into the coating by heating to high temperature and cooling quickly [38,39]. These elements would inter-diffuse and recombine to form some new phases after annealing.

### 3.4. Microhardness of Coatings

Figure 10 shows the microhardness of different coatings and the compacted graphite cast iron. The microhardness of the annealed coatings increased significantly. The highest hardness of the coating annealed at 1020 °C was  $902.4 \pm 79.9 \text{ HV}_{0.2}$ , which was much higher than the as-sprayed one with the microhardness of  $528.4 \pm 23.7 \text{ HV}_{0.2}$ . In comparison, the microhardness of the annealed coating was obviously higher than the flame re-melted one with the microhardness of  $599.4 \pm 89.7 \text{ HV}_{0.2}$ . Wen et al. [32] reported that the average microhardness of a vacuum re-melted coating was about 875 HV, which was 4% higher than the as-sprayed one. Li et al. [28] reported the coating re-melted by TIG process had an average hardness of 780 HV, which was higher than the as-sprayed one with the microhardness of 580 HV. The translation zone had a comparable microhardness in the three annealed coatings. Moreover, the microhardness of the translation zone was lower than those of the as-sprayed coating and all three annealed ones, while it was higher than that of the compacted graphite iron substrate. All three translation zones had similar microstructures, so they had comparable microhardness values.

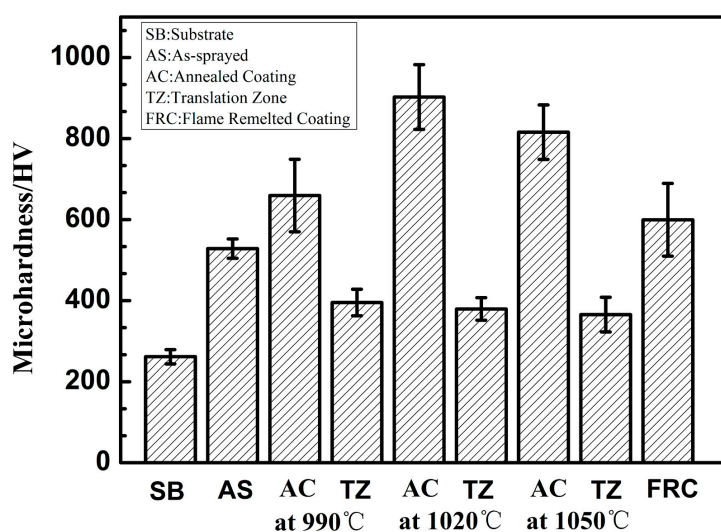


Figure 10. Microhardness of the coatings and the substrate.

Although the post-treatment processes to re-melt the coating were different, the microhardness values of the re-melted coatings were enhanced a lot, as compared with the as-sprayed one. There were two reasons for the higher microhardness of the re-melt coating. One was that the lamellar structure of the as-sprayed coating was eliminated after annealing, which decreased the pores and cracks and increased the density of the coating. Moreover, the diffused elements formed a bright translation zone, which is often considered as the feature of metallurgical bonding beneficial to improve the interface strength [28]. The other one was that the complexity of NiCrBSi alloy enabled different types of borides, carbides and silicides to form hard phases with nickel and chromium, such as  $\text{Ni}_2\text{B}$ ,  $\text{Ni}_{31}\text{Si}_{12}$ ,  $\text{Cr}_7\text{C}_3$  and  $\text{CrB}$ , which could increase the coating's hardness simultaneously [6]. When the annealing temperature was increased to 1050 °C, the coating's hardness decreased a little, as compared to the annealed one at 1020 °C. The translation zone thickness increased to 1145  $\mu\text{m}$ , and the nickel coating's thickness decreased to 161  $\mu\text{m}$  as compared to the as-sprayed thickness of 210  $\mu\text{m}$ . Moreover, nickel and chromium elements diffused into the translation zone, which would lead to the decrease of nickel and chromium contents in the coating. Therefore, the hardness would decrease a little but would still be higher than the annealed one at 990 °C.

### 3.5. Adhesion Strength

Table 6 shows the adhesion strength of the as-sprayed nickel-based coating and the annealed ones. The adhesion strength of the as-sprayed coating was 33 MPa. The coating's adhesion strength increased to 163 MPa after being annealed at 1050 °C for 20 min, which was about five times the adhesion strength of the as-sprayed one. Meanwhile, the annealed coating at 1050 °C for 20 min had a high-temperature adhesion strength of 146 MPa at 500 °C.

Table 6. Adhesion strength of the coatings.

Adhesion Strength/MPa Deposit	As-Sprayed	Annealed		
		990 °C	1020 °C	1050 °C
Room Temperature (RT)	33 ± 1.4	132 ± 10	142 ± 13	163 ± 13
500 °C	-	127 ± 8	121 ± 10	146 ± 6

Meng et al. [40] reported that the adhesion strength of a plasma-sprayed CoNiCrAlY coating increased to 66 MPa from the as-sprayed one of 28 MPa after vacuum heat treatment for 10 h. The inter-diffusion of elements resulted in the formation of metallurgical bonding between the

deposited splats and the surface of the substrate during vacuum heat treatment, which would increase the adhesion strength of the coating. In this work, short-term diffusion led to better metallurgical bonding between coatings and substrate as well as higher adhesion strength as compared with Meng's annealing of a CoNiCrAlY coating [40]. Furthermore, B and Si would accelerate the diffusion of Ni and Cr to iron. Therefore, the adhesion strength was enhanced to a high level.

Figure 11 shows the fracture surface morphology of the coatings after adhesion strength testing. The as-sprayed coating fractured at the interface between the compacted graphite iron and nickel-based alloy coating, as seen in Figure 11a. Meanwhile, many fragments formed in the as-sprayed coating after adhesion strength testing, which reflected the relatively poor cohesion among particles in the as-sprayed coating. In comparison, the coating annealed at 990 °C for 20 min fractured in the transition zone after adhesion strength testing, as seen in Figure 11b, which corresponded to the higher adhesion strength than the as-sprayed one. Moreover, there were no small fragments in the fracture surface, which reflected the strengthened inner cohesion of the coatings. After vacuum annealing, the adhesion between compacted graphite iron and coating was enhanced greatly. Meanwhile, the inner cohesion of the coating was improved too with the particles' interfaces healing and higher hardness than the as-sprayed one.

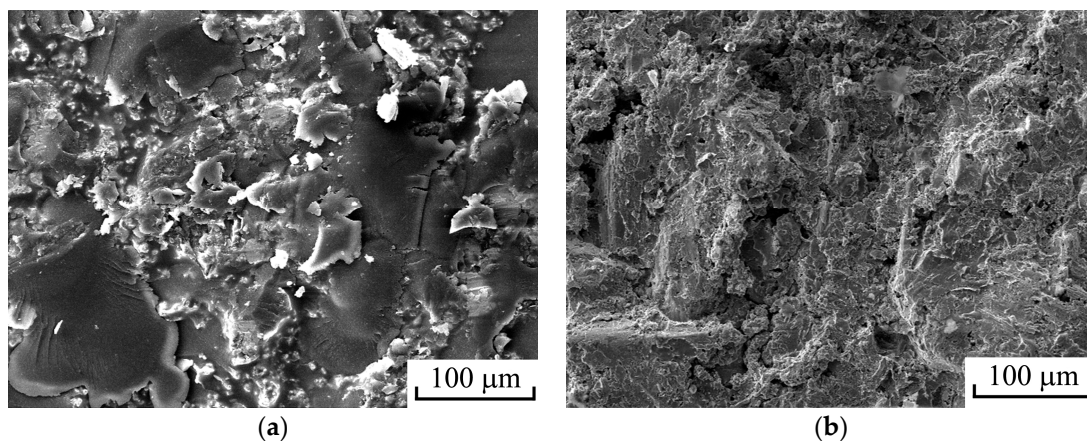


**Figure 11.** Fracture surface morphology of the coatings after adhesion strength test (a) and the as-sprayed coating (b) at 990 °C for 20 min.

#### 4. Conclusions

Vacuum annealing of plasma-sprayed nickel-based coatings on the compacted graphite cast iron RuT300 was investigated to improve the adhesion between coatings and substrate as well as the cohesion of the coatings. Nickel and chromium diffused between nickel-based alloy coatings and compacted graphite cast iron substrates during annealing at high temperature enhanced the adhesion, and a metallurgical transition zone formed with a thickness up to 1145 μm. The adhesion strengths at room temperature and 500 °C were increased to 163 and 146 MPa, respectively. After annealing, the cohesions were enhanced with the disappearance of particle interfaces, as compared to the as-sprayed one. The microhardness of the nickel-based alloy coating increased to 902 HV after annealing at 1050 °C for 20 min, as compared to the as-sprayed one of 528 HV.

**Author Contributions:** Conceptualization, P.G., M.L. and J.L.; methodology, Z.Y.; validation, B.C., T.X., Y.G. and S.Z.; writing—original draft preparation, P.G. and B.C.; writing—review and editing, P.G. and J.L.; and funding acquisition, J.L. All authors have read and agreed to the published version of the manuscript.

**Funding:** This work was funded by the National Natural Science Foundation of China under Grant 51771140; Key Project of Equipment Pre-search Field Fund under Grant 6140922010301; Shaanxi Key Science and Technology Innovation Team under Grant 2017KCT-05; The Youth Innovation Team of Shaanxi Universities: Metal Corrosion Protection and Surface Engineering Technology; Shaanxi Provincial Key Research and Development Project under Grant 2018GY-111 and 2019ZDLGY05-09; Local Serving Special Scientific Research Projects of Shaanxi

Provincial Department of Education under Grant 19JC022; Project of Yulin Science and Technology Bureau under Grant 2019-121.

**Acknowledgments:** We acknowledge Songsong Guo and Huibing Huo for their help in vacuum annealing.

**Conflicts of Interest:** The authors declare no conflict of interest.

## References

1. Wu, Y.; Li, J.P.; Yang, Z.; Guo, Y.C.; Ma, Z.J.; Liang, M.X.; Yang, T.; Tao, D. Creep behavior accompanying oxidation of compacted graphite cast iron. *Mater. Sci. Eng. A* **2018**, *723*, 174–181. [[CrossRef](#)]
2. Johansson, S.; Frennfelt, C.; Killinger, A.; Nilsson, P.H.; Ohlsson, R.; Rosen, B.G. Frictional evaluation of thermally sprayed coatings applied on the cylinder liner of a heavy duty diesel engine: Pilot tribometer analysis and full scale engine test. *Wear* **2011**, *273*, 82–92. [[CrossRef](#)]
3. Barbezat, G. Application of thermal spraying in the automobile industry. *Surf. Coat. Technol.* **2006**, *201*, 2028–2031. [[CrossRef](#)]
4. He, X.M.; Liu, X.B.; Wang, M.D.; Yang, M.S.; Shi, S.H.; Fu, G.Y.; Chen, S.F. Elevated temperature dry sliding wear behavior of nickel-based composite coating on austenitic stainless steel deposited by a novel central hollow laser cladding. *Appl. Surf. Sci.* **2011**, *258*, 535–541. [[CrossRef](#)]
5. Bobzin, K.; Ernst, F.; Zwick, J.; Schlaefer, T.; Cook, D.; Nassenstein, K.; Schwenk, A.; Schreiber, F.; Wenz, T.; Flores, G.; et al. Coating bores of light metal engine blocks with a nanocomposite material using the plasma transferred wire arc thermal spray process. *J. Therm. Spray Technol.* **2008**, *17*, 344–351. [[CrossRef](#)]
6. Liu, L.M.; Xu, H.F.; Xiao, J.K.; Wei, X.L.; Zhang, G.; Zhang, C. Effect of heat treatment on structure and property evolutions of atmospheric plasma sprayed NiCrBSi coatings. *Surf. Coat. Technol.* **2017**, *325*, 548–554. [[CrossRef](#)]
7. Wang, H.; Wang, H.W. Fabrication of self-lubricating coating on aluminum and its frictional behavior. *Appl. Surf. Sci.* **2007**, *253*, 4386–4389. [[CrossRef](#)]
8. Katsich, C.; Badisch, E. Effect of carbide degradation in a Ni-based hardfacing under abrasive and combined impact/abrasive conditions. *Surf. Coat. Technol.* **2011**, *206*, 1062–1068. [[CrossRef](#)]
9. Zhou, S.; Zeng, X.; Hu, Q.; Huang, Y. Analysis of crack behavior for Ni-based WC composite coatings by laser cladding and crack-free realization. *Appl. Surf. Sci.* **2008**, *255*, 1646–1653. [[CrossRef](#)]
10. Kim, D.J.; Lee, G.G.; Kim, D.J.; Jeong, S.J. Material characterization of Ni base alloy for very high temperature reactor. *J. Mater. Sci. Technol.* **2013**, *29*, 1184–1190. [[CrossRef](#)]
11. Serres, N.; Hlawka, F.; Costil, S.; Langlade, C.; Machi, F. An investigation of the mechanical properties and wear resistance of NiCrBSi coatings carried out by in situ laser remelting. *Wear* **2011**, *270*, 640–649. [[CrossRef](#)]
12. Liu, J.W.; Bolot, R.; Costil, S.; Planche, M.P. Transient thermal and mechanical analysis of NiCrBSi coatings manufactured by hybrid plasma spray process with in-situ laser remelting. *Surf. Coat. Technol.* **2016**, *292*, 132–143. [[CrossRef](#)]
13. Zhang, X.C.; Xu, B.S.; Wu, Y.X.; Xuan, F.Z.; Tu, S.T. Porosity, mechanical properties, residual stresses of supersonic plasma-sprayed Ni-based alloy coatings prepared at different powder feed rates. *Appl. Surf. Sci.* **2008**, *254*, 3879–3889. [[CrossRef](#)]
14. Huang, S.M.; Sun, D.Q.; Wang, W.Q.; Xu, H.Y. Microstructures and properties of in-situ TiC particles reinforced Ni-based composite coatings prepared by plasma spray welding. *Ceram. Int.* **2015**, *41*, 12202–12210. [[CrossRef](#)]
15. Gao, P.H.; Yang, G.J.; Cao, S.T.; Li, J.P.; Guo, Y.C.; Yang, Z. Heredity and variation of hollow structure from powders to coatings through atmospheric plasma spraying. *Surf. Coat. Technol.* **2016**, *305*, 76–82. [[CrossRef](#)]
16. Šárka, H.; Eva, S.; Marek, V.; Jan, S. Properties of NiCrBSi coating, as sprayed and remelted by different technologies. *Surf. Coat. Technol.* **2014**, *253*, 14–26. [[CrossRef](#)]
17. Gao, P.H.; Jia, H.; Wang, W.; Chen, B.Y.; Guo, Y.C.; Yang, Z.; Wang, J.D. Progress of Pore Structure Characterization of Thermal Sprayed Coatings. *Rare Met. Mater. Eng.* **2019**, *48*, 3055–3070.
18. Tyagi, R.; Xiong, D.S.; Li, J.; Dai, J. Elevated temperature tribological behavior of Ni based composites containing nano-silver and h-BN. *Wear* **2010**, *269*, 884–890. [[CrossRef](#)]
19. Gao, P.H.; Chen, B.Y.; Wang, W.; Jia, H.; Li, J.P.; Guo, Y.C.; Yang, Z. Simultaneous increase of friction coefficient and wear resistance through HVOF sprayed WC-(nano WC-Co). *Surf. Coat. Technol.* **2019**, *363*, 379–389. [[CrossRef](#)]

20. Karaoglanli, A.C.; Oge, M.; Doleker, K.M.; Hotamis, M. Comparison of tribological properties of HVOF sprayed coatings with different composition. *Surf. Coat. Technol.* **2017**, *318*, 299–308. [[CrossRef](#)]
21. Yu, T.; Deng, Q.; Dong, G.; Yang, J. Effects of Ta on microstructure and microhardness of Ni laser clad coating. *Appl. Surf. Sci.* **2011**, *257*, 5098–5103. [[CrossRef](#)]
22. Li, C.J.; Yang, G.J.; Li, C.X. Development of particle interface bonding in thermal spray coatings: A Review. *J. Therm. Spray Technol.* **2013**, *22*, 192–206. [[CrossRef](#)]
23. Pershin, V.; Lufitha, M.; Chandra, S.; Mostaghimi, J. Effect of substrate temperature on adhesion strength of plasma-sprayed nickel coatings. *J. Therm. Spray Technol.* **2003**, *12*, 370–376. [[CrossRef](#)]
24. Nicolas, S.; Françoise, H.; Costil, S.; Cécile, L.; Frédérique, M. Corrosion properties of in situ laser remelted NiCrBSi coatings comparison with hard chromium coatings. *J. Mater. Process. Technol.* **2011**, *211*, 133–140. [[CrossRef](#)]
25. Liu, J.W.; Wang, Y.; Costil, S.; Bolot, R. Numerical and experimental analysis of molten pool dimensions and residual stresses of NiCrBSi coating treated by laser post-remelting. *Surf. Coat. Technol.* **2017**, *318*, 341–348. [[CrossRef](#)]
26. Felgueroso, D.; Vijande, R.; Cuetos, J.M.; Tucho, R.; Hernández, A. Parallel laser melted tracks: Effects on the wear behaviour of plasma-sprayed Ni-based coatings. *Wear* **2008**, *264*, 257–263. [[CrossRef](#)]
27. Kamara, A.M.; Davey, K. A numerical and experimental investigation into residual stress in thermally sprayed coatings. *Int. J. Solids Struct.* **2007**, *44*, 8532–8555. [[CrossRef](#)]
28. Li, G.L.; Li, Y.L.; Dong, T.S.; Fu, B.G.; Wang, H.D.; Zhao, X.D.; Zhou, X.K. Microstructure and interface characteristics of NiCrBSi thick coating remelted by TIG process. *Vacuum* **2018**, *256*, 440–448. [[CrossRef](#)]
29. Tian, J.J.; Yao, S.W.; Luo, X.T.; Li, C.X.; Li, C.J. An effective approach for creating metallurgical self-bonding in plasma-spraying of NiCr-Mo coating by designing shell-core-structured powders. *Acta Mater.* **2016**, *110*, 19–30. [[CrossRef](#)]
30. Bergant, Z.; Grum, J. Quality improvement of flame sprayed, heat treated, and remelted NiCrBSi coatings. *J. Therm. Spray Technol.* **2008**, *18*, 380–391. [[CrossRef](#)]
31. Bergant, Z.; Trdan, U.; Grum, J. Effect of high-temperature furnace treatment on the microstructure and corrosion behavior of NiCrBSi flame-sprayed coatings. *Corros. Sci.* **2014**, *88*, 372–386. [[CrossRef](#)]
32. Wen, Z.H.; Bai, Y.; Yang, J.F.; Huang, J.; Zhang, L. Effect of vacuum remelting on microstructure and wear resistance of NiCrMoY coatings deposited by supersonic atmospheric plasma spraying. *Surf. Coat. Technol.* **2015**, *281*, 62–67. [[CrossRef](#)]
33. Guo, H.J.; Li, B.; Lu, C.; Zhou, Q.; Jia, J.H. Effect of WC-Co content on the microstructure and properties of NiCrBSi composite coatings fabricated by supersonic plasma spraying. *J. Alloys Compd.* **2019**, *789*, 966–975. [[CrossRef](#)]
34. Sidhu, T.S.; Prakash, S.; Agrawal, R.D. A comparative study of hot corrosion resistance of HVOF sprayed NiCrBSi and Stellite-6 coated Ni-based superalloy at 900 °C. *Mater. Sci. Eng. A* **2007**, *445*, 210–218. [[CrossRef](#)]
35. Wen, Z.H.; Bai, Y.; Yang, J.F.; Huang, J. Corrosion resistance of vacuum remelted Ni60-NiCrMoY alloy coatings. *J. Alloys Compd.* **2017**, *711*, 659–669. [[CrossRef](#)]
36. Rachida, R.; Bachir, E.I.K.; Fabienne, D. Microstructure and mechanical characterization of NiCrBSi alloy and NiCrBSi-WC composite coatings produced by flame spraying. *Mater. Sci. Eng. B* **2019**, *241*, 13–21. [[CrossRef](#)]
37. Yu, J.; Song, B.; Liu, Y.C. Microstructure and wear behaviour of Ni-based alloy coated onto grey cast iron using a multi-step induction cladding process. *Results Phys.* **2018**, *10*, 339–345. [[CrossRef](#)]
38. Żórawski, W.; Skrzypek, S.J. Tribological properties of plasma and HVOF-sprayed NiCrBSi-Fe<sub>2</sub>O<sub>3</sub> composite coatings. *Surf. Coat. Technol.* **2013**, *220*, 282–289. [[CrossRef](#)]
39. Li, Y.L.; Dong, T.S.; Li, G.L.; Wang, H.D.; Fu, B.G.; Zheng, X.D.; Zhou, X.K. Microstructure and mechanical property of Ni-based thick coating remelted by gas tungsten arc. *Vacuum* **2018**, *155*, 260–269. [[CrossRef](#)]
40. Meng, G.H.; Zhang, B.Y.; Liu, H.; Yang, G.J.; Xu, T.; Li, C.X.; Li, C.J. Vacuum heat treatment mechanisms promoting the adhesion strength of thermally sprayed metallic coatings. *Surf. Coat. Technol.* **2018**, *344*, 102–110. [[CrossRef](#)]

